FERROELECTRICS

Toroidal polar topology in strained ferroelectric polymer

Mengfan Guo[1], Changqing Guo[2], Jian Han[1], Shulin Chen[3], Shan He[1], Tongxiang Tang[1], Qian Li[1,4], Joseph Strzalka[4], Jing Ma[1], Di Yi[1], Ke Wang[1], Ben Xu[1], Peng Gao[3], Houbing Huang[5], Long-Qing Chen[6], Shujun Zhang[7], Yuan-Hua Lin[1], Ce-Wen Nan[1]*, Yang Shen[1,8]*

Polar topological texture has become an emerging research field for exotic phenomena and potential applications in reconfigurable electronic devices. We report toroidal topological texture self-organized in a ferroelectric polymer, poly(vinylidene fluoride-*ran*-trifluoroethylene) [P(VDF-TrFE)], that exhibits concentric topology with anticoupled chiral domains. The interplay among the elastic, electric, and gradient energies results in continuous rotation and toroidal assembly of the polarization perpendicular to polymer chains, whereas relaxor behavior is induced along polymer chains. Such toroidal polar topology gives rise to periodic absorption of polarized far-infrared (FIR) waves, enabling the manipulation of the terahertz wave on a mesoscopic scale. Our observations should inform design principles for flexible ferroic materials toward complex topologies and provide opportunities for multistimuli conversions in flexible electronics.

Manipulation of spin, charge, orbit, and lattice degrees of freedom has led to numerous key discoveries in the past few decades, such as multiferroics (*1*–*3*), colossal magnetoresistance (*4*, *5*), and high-temperature superconductors (*6*, *7*). Assembly of real-space order parameters into toroidal topological patterns, such as magnetic skyrmions (spin) (*8*, *9*), polar vortices (charge) (*10*), and polar skyrmions (charge) (*11*), has been the topic of extensive research. The response of the toroidal moment for these topologies to external stimuli is expected to give rise to pyrotoroidic effects, piezotoroidic effects, electric field control of chirality (*12*), and other emerging phenomena. Toroidal polar topologies have been observed in ferroelectric oxides, including strained $PbTiO_3$ films (*13*) and superlattices of alternating $PbTiO_3$/$SrTiO_3$ layers (*10*–*12*). The closure of dipolar vector flux is caused by the competition among elastic, electric, and gradient energies, which involves the interplay of charge, orbital, and lattice degrees of freedom.

Organic ferroelectrics are interesting materials for applications because they can be solution processed, are lower in cost, and may have better flexibility than ceramic ferroelectrics (*14*–*16*). The most commonly studied organic ferroelectric system is poly(vinylidene fluoride) (PVDF) and its binary and ternary copolymers (*17*–*20*). The primary dipolar moments of PVDF are induced by alternating -CF_2 and -CH_2 groups along the polymer chains, whereas the permanent dipoles perpendicular to the polymer chain can be switched by electric field through crankshaft rotation about the chain axis (*21*). However, toroidal polar topology has never been observed in ferroelectric polymers. The origin of dipolar moments in PVDF is different from their oxide counterparts. The semicrystalline nature of PVDF leads to a large portion of amorphous phases with randomly distributed chains, hindering the formation of long-range polar order. This raises the question of whether toroidal polar topology can ever exist in ferroelectric polymers and the driving forces for the topology formation can be identified.

We demonstrate the emerging toroidal polar topology in a ferroelectric polymer, poly(vinylidene fluoride-*ran*-trifluoroethylene) [P(VDF-TrFE)]. The effective alignment of the P(VDF-TrFE) lamellar crystals with their interchain dipoles perpendicular to the polymer chains self-organizing into a concentric pattern generates a toroidal polar topology. In addition, intrachain ferroelectricity parallel to the polymer chains is observed in P(VDF-TrFE), giving rise to the observed ferroelectric relaxation behavior in the aligned lamellae. The two orthogonal polarizations are coupled to each other, inducing a toroidal distribution of intrachain piezoelectricity. The biaxial strain induced by the Curie transition of P(VDF-TrFE) is responsible for the toroidal order and relaxor behavior because the local strain and elastic energy are redistributed with the flattened energy landscape of polarization states. In addition, the P(VDF-TrFE) lamellae with toroidal polar topology exhibit spatially periodic absorption on terahertz wave, which can be used to realize high-resolution terahertz raster and spatial light modulator. Our observations provide insight and design principles for integrating complex topologies into flexible materials, and also show opportunities for multistimuli conversions in flexible electronics.

By incorporating trifluoroethylene (TrFE) groups into PVDF, P(VDF-TrFE) exhibits a dominant crystalline β phase with an all-trans conformational sequence, leading to the strongest ferroelectricity among the PVDF family. The copolymer tends to crystallize into pseudohexagonal (orthorhombic), large-aspect-ratio lamellae with polymer chains parallel to the lamellar normal (the *c* axis) (*22*). The interchain dipoles of P(VDF-TrFE), which we attributed to the electronegativity difference between the H and F atoms, are induced perpendicular to the polymer chains. As illustrated at the bottom layer of Fig. 1A, such a configuration leads to the spontaneous electrical polarizations (straight arrows with blue-to-red gradient color) lying in the in-plane directions (*ab* plane) of the lamellae. Therefore, these dipoles could rotate substantially in the lamellar plane (Fig. 1A, circular arrow), which is an additional degree of freedom that is not possible to obtain in either oxide or other molecular ferroelectric materials (*23*, *24*). This degree of freedom might be a different approach to inducing toroidal order with high radial symmetry in a low symmetrical crystal lattice.

To understand the degree of freedom for in-plane dipolar rotation, we used a melt-recrystallization method (*25*, *26*) on spin-coated thin film to produce face-on lamellae with polymer chains vertically aligned and permanent polarizations lying in the in-plane directions of the film (Fig. 1A). We confirmed the vertical alignment of polymer chains with Fourier-transform IR spectroscopy (fig. S1), where an apparent parallel band (μ//*c* axis) occurs at 1400 cm^{-1} (*27*, *28*) under grazing-incident IR beam with electric field parallel to the film normal. Because of the rotational electrical polarizations distributed along the in-plane directions of the film, assembly of the dipoles can be characterized by in-plane piezo-response force microscopy (IP-PFM; Fig. 1). Exotic polar texture with hierarchical domain structure was observed in the face-on lamellae (Fig. 1, B to D), which consists of two parts, a central circle at the lamellar center and the surrounding ring-shaped bands (Fig. 1B). Angle-resolved IP-PFM images reveal that these two parts both consist of anticoupled stripe domains (fig. S2). In the central circle, the distribution of stripe domains reveals that the dominant orientations of polarizations are 58° to each other (Fig. 1C and fig. S2), which

[1]State Key Lab of New Ceramics and Fine Processing, School of Materials Science and Engineering, Tsinghua University, Beijing 100084, China. [2]School of Aerospace Engineering, Beijing Institute of Technology, Beijing 100081, China. [3]Electron Microscopy Laboratory and International Center for Quantum Materials, School of Physics, Peking University, Beijing 100871, China. [4]X-ray Science Division, Argonne National Laboratory, Lemont, IL 60439, USA. [5]Advanced Research Institute of Multidisciplinary Science, Beijing Institute of Technology, Beijing 100081, China. [6]Department of Materials Science and Engineering, The Pennsylvania State University, University Park, State College, PA 16802, USA. [7]Institute for Superconducting and Electronic Materials, Australian Institute for Innovative Materials, University of Wollongong, Wollongong, New South Wales 2500, Australia. [8]Center for Flexible Electronics Technology, Tsinghua University, Beijing 100084, China.
*Corresponding author. Email: cwnan@mail.tsinghua.edu.cn (C.-W.N.); shyang_mse@mails.tsinghua.edu.cn (Y.S)

indicates that the polarizations are mainly aligned along the [110] and [1$\bar{1}$0] directions in the pseudohexagonal lattice of P(VDF-TrFE). Conversely, in the surrounding ring-shaped bands, the polarizations continuously rotate about the center, forming chiral domains with uniformly distributed in-plane polarization (Fig. 1A). Furthermore, the chiral domains split into two types, with a 45° intersection angle between the net polarizations and band boundaries in clockwise or anticlockwise direction (Fig. 1, A and D), wherein we observed polarization discontinuity caused by the existence of head-to-head and tail-to-tail domain walls at the band boundaries (figs. S3 and S4). We transformed the circular pattern of the in-plane polarization with a two-dimensional fast Fourier transform (Fig. 1E), which also suggests the rotational symmetry of the in-plane polarizations. The bright green concentric circles in the low-frequency region correspond to the repetitively and alternately arranged bands, and the dark green shadow in the high-frequency region arises from the continuous rotation of real-space polarizations in the anti-coupled chiral domains.

To verify the existence of emergent order parameter in face-on P(VDF-TrFE) lamellae, we obtained detailed polarization distribution using phase-field simulation (*29*). On the basis of the polarization map (Fig. 1A), we then calculated the electric toroidal moment of the polar topology. Given the definition of electric toroidal moment (*30*–*32*) as $\vec{G}=\frac{1}{2V}\int_V \vec{r}\times\vec{P}\mathrm{d}V$, the electric toroidal moment along the z axis [G_z along the out-of-plane direction of the P(VDF-TrFE) face-on lamellae] is supposed to be substantially larger than those along x and y axes if toroidal order is present in the xy plane [x and y being in-plane directions of the P(VDF-TrFE) face-on lamellae]. By integrating the electric toroidal moment throughout the entire map and along a circular ring in the polarization map (fig. S5), we observed that G_z was one to two orders of magnitudes higher than G_x and G_y for both cases (table S2), justifying the existence of toroidal order within the face-on lamellae. The surface morphology in the atomic force microscopy (AFM) image (Fig. 1F) shows that the recrystallized P(VDF-TrFE) film consists of face-on lamellae with large lateral size (~50 μm) when film thickness is controlled around 100 nm. We observed the toroidal polar topology in all of these face-on lamellae (Fig. 1G). We also observed very similar yet much weaker signals using out-of-plane (OOP) PFM in the as-grown film (fig. S6). The IP-PFM scanning on thin film with edge-on lamellae (lamellar face perpendicular to film plane with c axis parallel to film plane) that we fabricated (*33*) indicates that the toroidal polar topology is distributed throughout the thickness of the face-on lamellae (fig. S7).

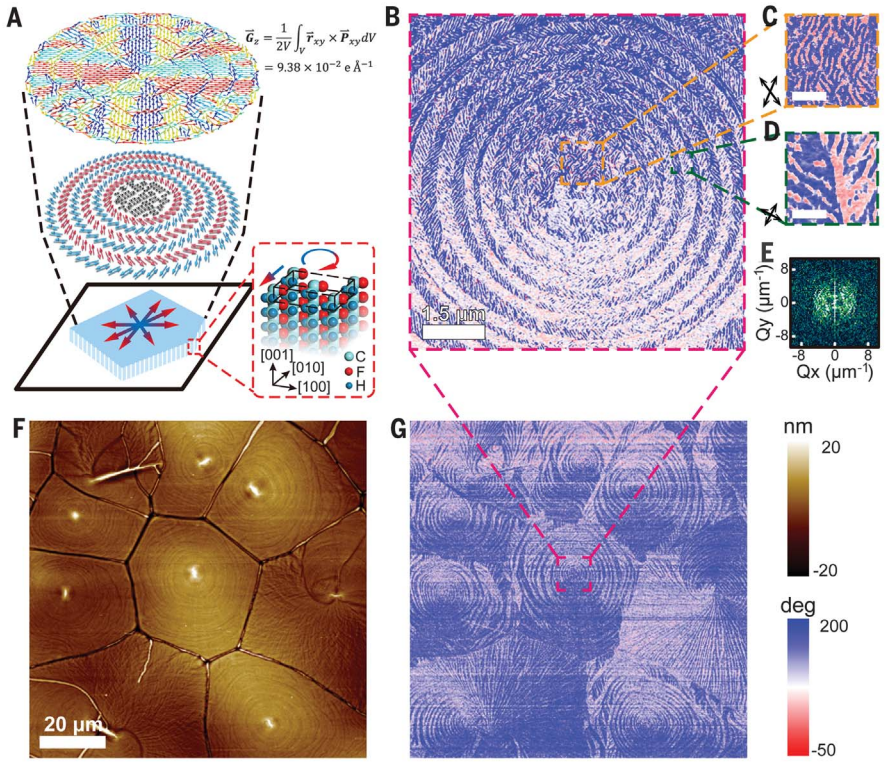

Fig. 1. Observation of toroidal polar topology. (**A**) Simulated polar topology (top) and schematic illustration of polarization (middle) and chain distribution (bottom) in a P(VDF-TrFE) lamella. Top layer is the simulated polarization map in a face-on lamella using the phase-field method. The electric toroidal moment of 9.38×10^{-2} e Å^{-1} along the z axis calculated accordingly suggests the existence of toroidal order in the polar topology. Middle layer is the schematic illustration of polarization distribution. In the central circle, the polarization states are mainly distributed along the <110> and <010> directions. In both types of bands, the polarization states show toroidal assembly uniformly oriented along in-plane directions. Bottom layer is the schematic illustration of a face-on lamella and its crystal orientation. The inset in the red dashed rectangle shows the oriented polymer chains and the lattice structure. In face-on lamellae, the polymer chains (denoted as the c axis) are aligned parallel to the lamellar normal. The straight arrows in blue-to-red gradient color denote the orientation of permanent dipoles. The circular arrow denotes the ability for these dipoles to rotate within the lamellar plane (*ab* plane) about the lamellar normal (c axis). (**B**) IP-PFM phase image showing hierarchical structures of the toroidal pattern [magnified from the area denoted by the red dashed square in (G)]. (**C**) IP-PFM phase image at the central circle [denoted by the orange dashed square in (B)], showing stripe domains in two dominant directions. Scale bar, 300 nm. (**D**) IP-PFM phase image at surrounding ring-shaped bands with band boundary [denoted by the green dashed square in (B)] showing the 45° intersection between stripes and band boundary in clockwise and anticlockwise direction. Scale bar, 150 nm. (**E**) Two-dimensional fast Fourier transform of (B) showing stronger concentric distribution in the low-frequency region and weaker shadow distribution in the high-frequency region. (**F**) Morphology of melt-recrystallized P(VDF-TrFE) consisting of face-on lamellae. (**G**) IP-PFM phase image of the same area in (F) exhibiting large-scale toroidal polar topologies in all lamellae.

The periodically banded structures (*34*–*36*) have often been observed in organic thin films during their melt-recrystallization processes, such as isotactic polystyrene (*37*), poly(L-lactide) (*38*), poly(ε-caprolactone) (*39*), and molecular semiconductors (*40*). The periodic surface topography is attributed to the competition between long-range mass transport from the surrounding melt and crystallization at the transformation front. We can use the same mechanism to explain the formation of the polar ring–shaped bands with chiral domains in P(VDF-TrFE) during recrystallization from melt. In the case of the nonpolar molecules and macromolecules, however, the amplitude of periodic height undulation is on the order of film thickness, whereas for polar P(VDF-TrFE), the amplitude of surface undulation at the banded region is more than one order of magnitude smaller than the film thickness (Fig. 1F and fig. S8). Unlike those nonpolar organics, the strong polarity of PVDF-based polymers has a substantial impact on their crystallization behavior (*41*). Therefore, we

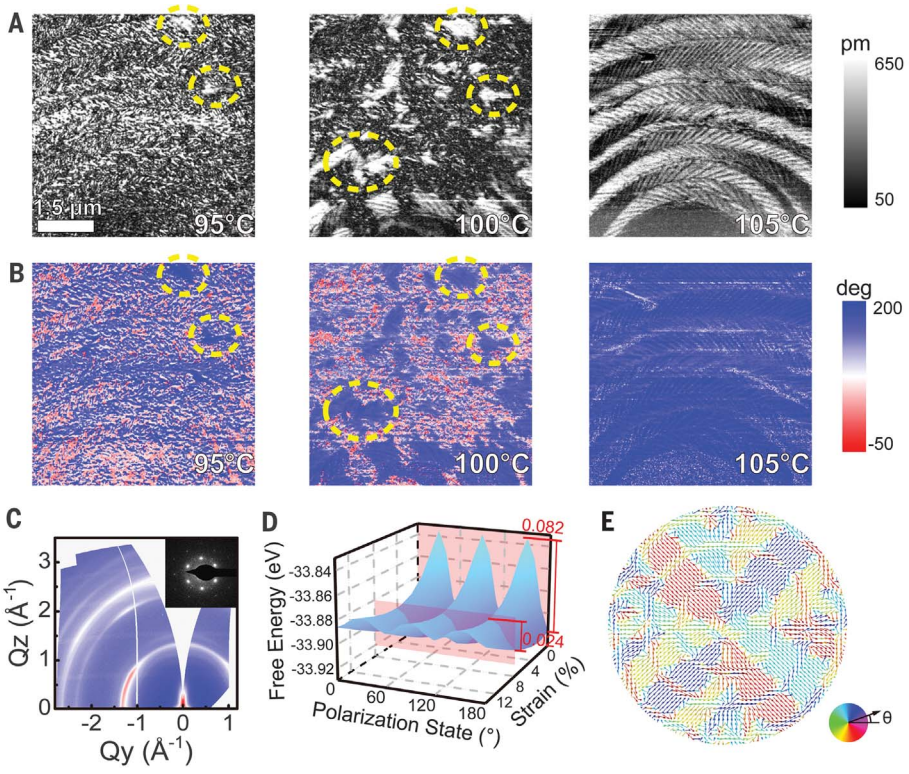

Fig. 2. Characterization and calculations of P(VDF-TrFE) lamellae. (**A** and **B**) Temperature-dependent IP-PFM (A) phase and (B) amplitude images of a face-on lamella. The yellow dashed circles denote several emerging paraelectric phase in the ferroelectric matrix. (**C**) GI-WAXS pattern of face-on lamellae. The main scattering arc appears at (Qy = −1.31 Å^{-1}, Qz = 0 Å^{-1}). Inset, SAED pattern of free-standing face-on lamellae. The pseudohexagonal pattern indicates that the face-on lamella is a single crystal with its ***c*** axis aligned parallel to the electron beam. (**D**) Energy levels of strained PVDF lattice at different polarization states. For simplification, instead of P(VDF-TrFE), β-phase PVDF chain is adopted, with [010] direction set as 0°. The lowest energy levels at 60°, 120°, and 180° correspond to stable polarization states along [110], [1$\bar{1}$0], and [0$\bar{1}$0], respectively. The free energy contrast of the strain free lattice is 0.082 eV, which reduces to 0.024 eV upon an 8% tensile strain, denoted by the red planes. (**E**) Polarization map of a face-on P(VDF-TrFE) lamella under tensile strain of 7.30% by phase-field simulations. Each arrow represents the direction of in-plane polarization as depicted in the colored disk. The diameter of simulated map is 180 nm.

believe that the permanent dipoles in banded structures is responsible for the partially alleviated surface undulation, resulting in the toroidal polar topology with less undulation amplitude in face-on P(VDF-TrFE) lamellae.

The formation of the toroidal polar topology is closely associated with the melt-recrystallization treatment, and thus we sought to understand the thermal evolution of the polar topology in P(VDF-TrFE) thin films. Two phase transitions exist in P(VDF-TrFE) when heating, the ferroelectric-paraelectric phase transition at ~100°C and the paraelectric-disordered (molten) phase transition at ~135°C (*42*). We used in situ, temperature-dependent PFM to observe the polar topology in the face-on lamellae as a function of temperature. To prevent the electrical interference of PFM tips on paraelectric face-on lamellae upon the transition to ferroelectric phase, we performed all of the observations upon heating. Considering that P(VDF-TrFE) can be reversibly transformed among the ferroelectric, paraelectric, and disordered phases with thermal hysteresis (*18*), we believe that the evolution during heating could reversibly happen upon cooling. The ferro-to-paraelectric transition starts at 95°C, accompanied by the emerging paraelectric regions (Fig. 2, A and B, figs. S9 and S10). Increasing the temperature further induces the growth of the paraelectric phase. Notwithstanding the disappearance of antiparallel stripe domains >105°C (red color domains disappear in Fig. 2B at 105°C), the toroidal topology still exists and can be clearly observed in paraelectric face-on lamellae (Fig. 2A at 105°C). The paraelectric phase with disordered permanent dipoles is more responsive than the ferroelectric phase, which is contradictory to the concept that the paraelectric phase does not exhibit piezoelectricity. However, recent observations show the paraelectric and high-temperature P(VDF-TrFE) adopting 3/1-helical chain conformation has a distortive degree of freedom (*43*). This structure is thought to account for the enhanced responsivity and more pronounced toroidal assembly observed at elevated temperatures. When we raise the temperature to >110°C, the topology gradually weakens from the central circle of the face-on lamellae, and vanishes at 140°C, where the paraelectric phase completely changes to the disordered phase (fig. S11). We conclude from these observations that the toroidal order starts to form in the paraelectric phase at elevated temperature, whereas the ferroelectric order is assembled during the subsequent cooling to ferroelectric phase.

The continuous rotation of ferroelectric polarizations provides a solid foundation for the combination of ferroelectric and toroidal order. The measurements on crystalline structure and computation on corresponding free energy suggest that large biaxial tensile strain in the face-on lamellae stabilizes the polarization states along all the in-plane directions. We observed biaxial strain of 7.3% in P(VDF-TrFE) film with face-on lamellae by measuring the grazing-incident wide angle x-ray scattering (GI-WAXS) and selected area electron diffraction (SAED). In the GI-WAXS pattern of face-on lamellae (Fig. 2C), the main scattering arc appears with its center at (Qy = −1.31 Å^{-1}, Qz = 0 Å^{-1}), corresponding to the (110)/(200) duplicate units. For the SAED pattern (Fig. 2C), we observed only pseudohexagonal diffraction points corresponding to (110)/(200) planes, which verifies that the *a* and *b* axes are oriented along in-plane directions. We obtained the (110)/(200) spacing from these patterns, which are 4.803 and 4.80 Å according to GI-WAXS and SAED patterns, respectively. These values are much larger than the (110)/(200) spacing of 4.457 Å measured in a strain-free reference sample (fig. S12). Thus, the enhanced spacing in the face-on lamellae reveals a biaxial tensile strain of 7.3%, because all the (hk0) planes are vertically aligned in the face-on lamellae. By moving the sample in steps around a few microns with the diameter of selected area around 190 nm, we observed no change in lattice spacing and orientation within one lamella (fig. S13). Electron diffractions with multiple tilting angles and aperture diameter as large as 3.8 μm (figs. S14 and S15) also show distinct pseudohexagonal diffraction points, demonstrating that the strain is uniform in a single-crystalline lamella. Thermal expansion contrast between P(VDF-TrFE) and rigid substrate can only account for ~1% of biaxial strain. Thus, other mechanisms should be responsible for such large strain.

The substantial changes in the lattice parameters during the Curie transition of P(VDF-TrFE) (*44*) could explain the large biaxial strain in face-on lamellae. By measuring the temperature-dependent x-ray diffraction of the strain-free P(VDF-TrFE) (fig. S16) near its

Curie point (~100°C in heating process), we can observe a large expansion along the *a* and *b* axes over the ferroelectric-to-paraelectric phase transition. Unlike Curie transition of ferroelectric oxides where polarization evolution is caused by the displacive movements of cations with minor lattice parameter change (*45*), the Curie transition of P(VDF-TrFE) involves substantial intramolecular changes in conformation sequence (*46*). For example, the disappearance of the all-trans sequence and the emergence of the gauche bond in paraelectric phase would lead to the rearrangement of the permanent dipoles. Consequently, the intermolecular interaction will be weakened and result in large expansion of interchain distance in the paraelectric phase of PVDF-based polymers while retaining the pseudo-hexagonal symmetry. During the Curie transition, the (110)/(200) lattice spacing increases from 4.48 Å in the ferroelectric phase to 4.93 Å in the paraelectric phase, accounting for a 9% biaxial shrinkage (close to the measured strain of 7.3%) during the paraelectric-to-ferroelectric transition. For a thin film with face-on lamellae where the *a* and *b* axes are oriented along the in-plane directions, a large biaxial tensile strain is introduced as the lamellae are clamped by the substrate (fig. S16). This clamping effect mainly relies on the inherent lattice change of the film, different from the lattice mismatch mechanism in epitaxially grown oxide films. The clamping effect is also revealed by the large-scale parallel stripes in face-on lamellae with large portion of gaps serving as strain-releasing sites when lamellar thickness is <60 nm (fig. S17).

To further explore the effect of strain on the in-plane ferroelectric polarization rotation, we performed first-principle calculations to examine the free energy of P(VDF-TrFE) film with different polarization orientations under different strain levels [figs. S18 to S21 (*29*)]. For the strain-free lattice (Fig. 2D), the chain rotation angles at 0°, 60°, and 120° with corresponding polarization states along [010], [110], and [1$\bar{1}$0] exhibit the lowest free energy level. These results are consistent with the pseudo-hexagonal symmetry of β-phase PVDF-based polymers. Deviation from these low-energy states induces substantial increases in free energy, which therefore does not favor the continuous rotation of polarizations to form the toroidal polar topology. When large tensile strain is applied, the barrier between energy minimum and maximum in the energy landscape reduces substantially, leading to an almost degenerate state as polarization rotates in the *ab* plane. For instance, with biaxial tensile strain of 8% (close to the measured value of 7.3%; Fig. 2D, red plane), the energy barrier between different polarization orientations reduces from 0.082 to 0.024 eV, almost one-fourth of the original value. The energy landscape should be further flattened when larger chain distance and lower interchain dipoles of P(VDF-TrFE) are considered. Thus, the strain-suppressed anisotropy within the *ab* plane could enable easier chain rotation for continuous rotation of polarizations. We note that this chain rotation degree of freedom is universal to all crystalline polymers.

For phenomenological understanding, we performed phase-field modeling to learn more about the effect of strain on the polarization distribution. The simulated polarization map of the wrinkled P(VDF-TrFE) nanodisk under a strain level of 7.30% (Figs. 1A and 2E) shows a toroidal polar topology with features similar to the IP-PFM phase image (Fig. 1B), where we observed the alternating bands with anti-coupled domains. We chose a P(VDF-TrFE) nanodisk with a diameter of 180 nm to simulate the polarization evolution because the spatial scale in the phase-field simulations (hundreds of nanometers) is much smaller than the scale of lamellae in the experiments (>10 μm). Therefore, the phase-field simulations are applied to qualitatively analyze the polarization distribution. In fact, the large strain induced by the paraelectric-to-ferroelectric phase transition changes the interplay between the electric and elastic energies (*22*). However, the toroidal assembly of polarizations is mainly attributed to the periodic undulation of the wrinkled surface, which redistributes the strain and consequent elastic energy in a concentric manner (fig. S22), affecting the local interplay among elastic, electric, and gradient energies. Thus, the film thickness plays an important role as it determines the application and redistribution of strain by controlling the film morphology (fig. S17). With the larger tensile strain applied, the polarizations rotate more continuously as the lateral size of anticoupled domains decreases with increasing strains (fig. S23), which is consistent with the degenerate free energies of all polarization states calculated by the first-principle calculations. Therefore, strain in the face-on lamellae is critical for the development of toroidal polar topology and enables continuous rotation of the in-plane polarizations in face-on P(VDF-TrFE) lamellae.

The flat energy landscape based on first-principle calculations suggests that tensile strain facilitates the chain rotation degree of freedom. Recent work on ferroelectric nylon also shows that the introduction of conformational defects can enable easier chain rotation and effectively induce relaxor-like behavior by suppressing the interchain hydrogen bond (*47*). Analogous to this, we believe that the relaxation behavior can also exist in face-on P(VDF-TrFE) lamellae. Using a customized holder for soft thin film [fig. S24 (*29*)], we obtained temperature-dependent dielectric spectra of the face-on lamellae (fig. S25). We measured the room temperature dielectric

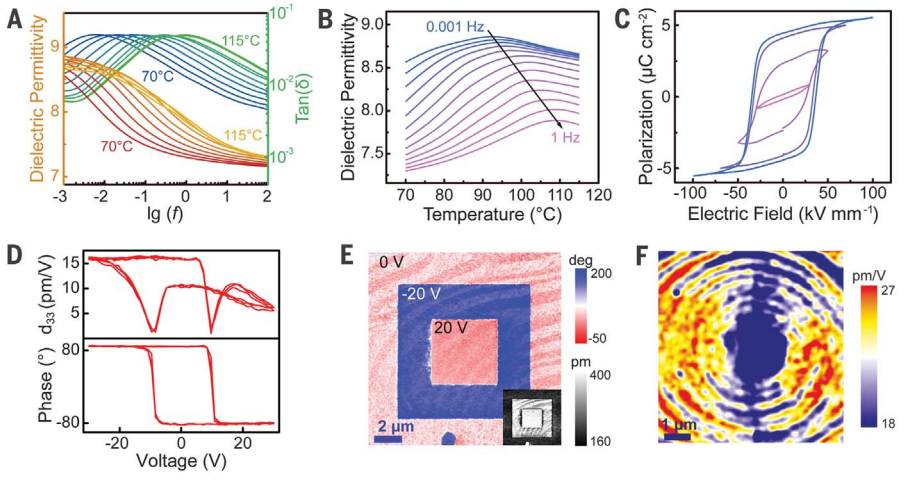

Fig. 3. Properties of face-on P(VDF-TrFE) lamellae. (**A**) Temperature-dependent broadband dielectric spectroscope of face-on lamellae from 70 to 115°C. A relaxation peak related to ferroelectricity along the chain direction at ultra-low-frequency shifts to higher region with increasing temperature. (**B**) Temperature-dependent profiles of dielectric peaks along chain direction showing evident relaxor behavior. (**C**) P-E loops of multilayered face-on lamellae from Sawyer-Tower circuit. (**D**) PFM-switching spectrum of single-layered face-on lamellae measured by interferometric displacement sensor (IDS). (**E**) PFM phase image of face-on lamellae poled by conducting tip. The blue area was poled by −20 V. The red area with square shape at the center was poled by 20 V. The outer red area was unpoled. Inset is the PFM amplitude image of the same area. The negatively poled area shows similar amplitude to the positively poled one. (**F**) PFM switching spectra mapping of face-on lamellae. Areas with stronger piezo responses are organized into a concentric pattern showing strong coupling between the toroidal topology and the ferroelectricity along the chain direction.

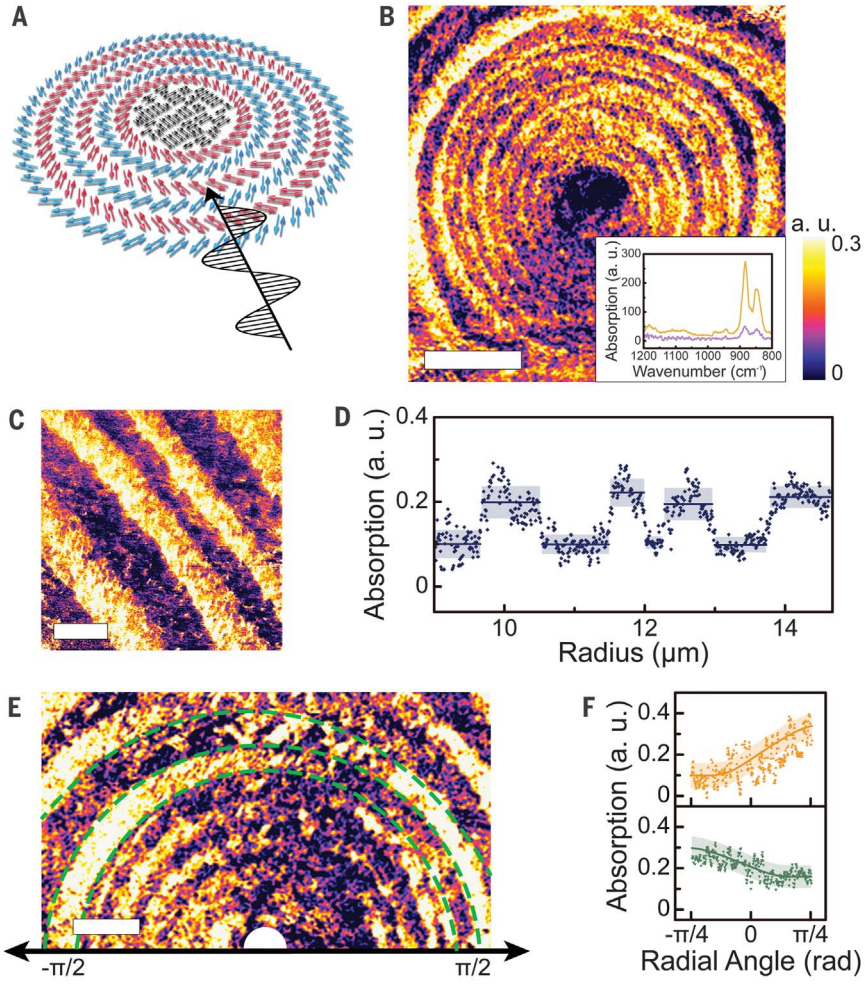

Fig. 4. Spatially periodic absorption of FIR waves. (**A**) Schematic illustration of the configuration of polarized IR beam and face-on lamellae in AFM-IR measurements. (**B**) Absorption mapping of face-on lamellae exhibiting toroidal topology on an FIR wave with wavenumber of 880 cm^{-1}. Inset, AFM-IR spectra measured at neighboring bands, showing one-order-of-magnitude contrast. Scale bar, 3 μm. (**C** and **D**) FIR absorption (C) mapping and (D) profile along radius direction in polar coordinate showing alternate low and high absorption level in neighboring bands. Scale bar, 100 nm. (**E** and **F**) FIR absorption mapping (E) and profiles (F) along the radial angle direction in polar coordinate showing changes in absorption level within the same band; absorption distributions in the neighboring bands are inverse because of their orthogonal polarization states. Scale bar, 100 nm.

permittivity of the face-on P(VDF-TrFE) to be ~7 and identified a relaxation peak at low frequency at elevated temperatures. Therefore, we conducted temperature-dependent broadband dielectric spectroscope with frequency as low as 10^{-3} Hz (Fig. 3A), showing typical relaxation behavior in the temperature-dependent profiles (Fig. 3B). We note that this relaxation at low frequency should not be attributed to the space charge polarization because the slope of loss tangent versus frequency in logarithmic scale is −0.283, much smaller than −1, which is the main characteristic of ionic relaxation. We further fitted the experimental data to the Vogel-Fulcher law (*20*, *43*, *48*), confirming the relaxor nature in the strained face-on lamellae (fig. S26). The fitting yielded a freezing temperature of 85.63°C, which could rationalize the emergence of the distinct ferroelectric domains observed at room temperature (Fig. 1B). Conversely, the strain-free edge-on lamellae show no relaxation behavior over the entire frequency range (figs. S27 and S28). It is worth noting that the dielectric peak in fig. S27 around 10^7 Hz is attributed to the relaxation of interchain dipoles perpendicular to the polymer chains. For the face-on lamellae with vertically aligned polymer chains, the interchain dipoles are lying in the film plane and should be undetectable during the dielectric measurements. However, we can still measure a dielectric permittivity of ~7, which should be attributed to the dielectric response along the polymer chains. The special chain alignment in face-on lamellae exposes the polymer chains parallel to the electric field, and thus facilitates the dielectric response of the carbon backbone along the *c*-axial direction. Given the large size of the carbon backbone along polymer chains (100 nm, ~1000 atoms) compared with the rotational -CH_2-CF_2- groups about the *c* axis (~0.3 nm), this mechanism will also explain the relaxation process at low frequencies, as show in Fig. 3A. The relaxor behavior is consistent with degenerate energy landscape with applied strain (Fig. 2D), which indicates that the relaxor property is associated with the tensile strain. Analogous to the bulky side groups (*19*) and electron irradiation (*49*) in PVDF-based polymers that break the long-range ferroelectric order, the biaxial strain induced by the Curie transition may also serve as a new route to transform normal ferroelectric P(VDF-TrFE) into relaxors.

Given the robust dielectric response along the *c* axis of the face-on P(VDF-TrFE) lamellae, we further explored the ferroelectricity along the *c* axis, the existence of which is still under debate. Park *et al.* reported the polarization extinction in P(VDF-TrFE) film with face-on lamellae (*25*), whereas Lee *et al.* still observed a P-E hysteresis loop in P(VDF-TrFE) film with the same orientation (*26*). The dielectric behavior that we observed (Fig. 3B) is distinctly different from that of interchain dipoles (figs. S27 and S28), suggesting that the *c*-axial ferroelectricity could rely on the intramolecular dipolar behaviors of the long chains. We then verified the ferroelectricity along polymer chains by measuring polarization hysteresis loops using a Sawyer-Tower circuit (Fig. 3C). We obtained typical hysteresis loops in the film with stacking, multilayered face-on lamellae, where we found the saturated polarization (P_s) to be ~5 μC cm^{-2}. This value was ~50% lower than the edge-on P(VDF-TrFE) lamellae (*18*) and similar to the value reported by Lee *et al.* (*26*). Furthermore, we used PFM equipped with an interferometric displacement sensor to measure the piezoelectric d_{33} of the face-on lamellae. We measured a butterfly-shaped curve with maximum d_{33} of ~15 pm V^{-1} (Fig. 3D), evidence of piezoelectricity along the *c* axis. By applying DC bias on the scanning tip, we can also switch the ferroelectric polarization along the *c* axis. As shown in the OOP-PFM scanning (Fig. 3E), both the negative and positive biases can activate the piezoelectric response (Fig. 3E, inset) with opposite phase. Our observations confirmed that the dipoles along the chain direction (*c* axis in an orthogonal lattice) can be switched between bistable states. To eliminate the interference from charge injection, we characterized the polarization retention of the face-on P(VDF-TrFE)

lamellae (fig. S29). The phase and amplitude of the switched areas remain unchanged after 150 min, confirming that the ferroelectric switching along the *c* axis of the face-on P(VDF-TrFE) lamellae was triggered upon the application of a tip voltage. Ultimately, ring-shaped reinforced regions with similar pattern to a toroidal topology were obtained by mapping the switching spectra of face-on lamella (Fig. 3F). Between the two types of chiral domains, one of them exhibits a 50% higher piezoelectric response. Our observations provide convincing evidence for ferroelectricity and piezoelectricity along the polymer chain direction (the *c* axis of the face-on lamellae) in the PVDF-family ferroelectric polymer materials. Furthermore, the in-plane (*ab* plane) toroidal polar topology is strongly coupled with the out-of-plane ferroelectricity along *c* axis according to the concentric distribution of *c*-axial piezoelectric coefficient.

The strong coupling between ferroelectric polarization and toroidal polar topology has great potential for multifunctional coupling in our films. Bulk P(VDF-TrFE) or its thick films were reported to exhibit macroscopic selective absorption on IR and terahertz waves (*50*–*53*). Considering that the scale of face-on lamellae (10-50 μm) and the toroidal bands (0.1 to 1 μm) are within the range of the terahertz wavelength (0.1 to 10 THz, 30 to 0.3 μm), we expect the toroidal polar topology to have the ability to microscopic manipulation on terahertz waves. This might enable terahertz raster and spatial light modulator (*54*, *55*) with high spatial resolution. Therefore, we used an AFM equipped with tunable polarized IR beam (AFM-IR) to explore the potential application of the toroidal polar topology in terahertz optics. For face-on lamellae, the toroidal distribution of in-plane polarization could give rise to spatially resolved absorption modulation of IR waves. For the IR band of P(VDF-TrFE) in far-infrared (FIR) region at 880 cm^{-1} (26.4 THz), the absorption is caused by the IR excitation of the symmetric stretching of CF_2 groups, the transition dipoles of which are parallel to the in-plane ferroelectric polarizations [fig. S30 (*27, 28*)]. When a polarized FIR beam with electric field parallel to the film plane is projected to the face-on lamellae (Fig. 4A), the local absorptions of face-on lamellae continuously vary because of the alternated toroidal ferroelectric polarizations. We indeed observed the periodic absorption pattern of FIR beam on the toroidal topology (Fig. 4B). The IR absorption decreased by an order of magnitude (Fig. 4B, inset) as the local polarization is vertical to the electric field of polarized FIR beam. By contrast, when the FIR beam was polarized with electric field perpendicular to the in-plane directions of the face-on lamellae, the absorption level in face-on lamellae is uniform (fig. S31). Despite the switching of ferroelectric polarization along the chain direction, we observed no coupling between the OOP polarizations and OOP absorptions.

The face-on lamellae with toroidal polar topologies exhibit strong selective FIR absorption with spatial periodicity. In polar coordinates, because the polarization states are orthogonal in neighboring bands, the absorption level varies periodically along the radius directions (Fig. 4, C and D). The spatial period depends on the width of the surrounding bands (~ 200 nm). In addition, the polarization states in the same band at different radial angles will change as the local polarization rotates. For the two neighboring bands (Fig. 4, E and F, green dashed lines), the absorption in the upper one changes from low level (purple) to high level (yellow) when radial angle increases, whereas absorption in the lower band with orthogonal polarization varies in an opposite manner (yellow to purple). Therefore, the IR absorption of the face-on lamellae shows spatial periodicity along the radius and radial angle in the polar coordinates. In addition, when the incident beam power is magnified, the local temperature will become high enough to enable preferential decomposition in face-on lamellae (fig. S32). For the P(VDF-TrFE) film that we studied with toroidal polar topology, the featured scale of spatially periodic absorption is smaller than the terahertz wavelength by one to two orders of magnitudes, and the scale of lamella itself is within the range of terahertz wavelength. Face-on lamellae with these characteristic sizes are also expected to enable the design of selective Rayleigh scattering (in which the size of the scattering body is smaller than the wavelength by more than one order of magnitude) and Mie scattering (in which the size of the scattering body is close to the wavelength) in the terahertz region. We believe that this behavior has great potential for near-field interconversion for terahertz applications, including sensing (*52*), imaging (*56*), and communications (*57*, *58*).

The toroidal polar topology that we observed in P(VDF-TrFE) could be common to other organic ferroelectric systems because the strong lattice change during phase transition and the periodic surface topography after crystallization are common for molecular (macromolecular) crystals with low melting points. The manipulation of terahertz waves by toroidal and polar order through molecule orientation should also be applicable to other order-disorder ferroelectrics. In addition, because the ferroelectric properties of P(VDF-TrFE) change greatly near its morphotropic phase boundary (*20*), we would expect that the composition could be another dimension to manipulate the polar topology and the corresponding absorption behavior of electromagnetic waves. Thus, our observation of toroidal polar topology in a ferroelectric polymer may provide design opportunities for the interconversion of multistimuli in terahertz optics and enable the development of flexible device integrated with ferroic topology because the face-on lamellae can be fabricated directly on flexible substrates (see fig. S33).

REFERENCES AND NOTES

1. M. Dawber, K. M. Rabe, J. F. Scott, *Rev. Mod. Phys.* **77**, 1083–1130 (2005).
2. R. Ramesh, N. A. Spaldin, *Nat. Mater.* **6**, 21–29 (2007).
3. C. W. Nan, M. I. Bichurin, S. X. Dong, D. Viehland, G. Srinivasan, *J. Appl. Phys.* **103**, 031101 (2008).
4. A. J. Millis, *Nature* **392**, 147–150 (1998).
5. Y. Tokura, Y. Tomioka, *J. Magn. Magn. Mater.* **200**, 1–23 (1999).
6. E. Dagotto, *Rev. Mod. Phys.* **66**, 763–840 (1994).
7. Y. Tokura, N. Nagaosa, *Science* **288**, 462–468 (2000).
8. S. Mühlbauer *et al*., *Science* **323**, 915–919 (2009).
9. X. Z. Yu *et al*., *Nature* **465**, 901–904 (2010).
10. A. K. Yadav *et al*., *Nature* **530**, 198–201 (2016).
11. S. Das *et al*., *Nature* **568**, 368–372 (2019).
12. A. R. Damodaran *et al*., *Nat. Mater.* **16**, 1003–1009 (2017).
13. Y. L. Tang *et al*., *Science* **348**, 547–551 (2015).
14. R. B. Meyer, L. Liebert, L. Strzelecki, P. Keller, *J. Phys. Lett.* **36**, 69–71 (1975).
15. S. Horiuchi, Y. Tokura, *Nat. Mater.* **7**, 357–366 (2008).
16. P. P. Shi *et al*., *Chem. Soc. Rev.* **45**, 3811–3827 (2016).
17. A. J. Lovinger, *Science* **220**, 1115–1121 (1983).
18. T. Furukawa, *Phase Transit.* **18**, 143–211 (1989).
19. B. Neese *et al*., *Science* **321**, 821–823 (2008).
20. Y. Liu *et al*., *Nature* **562**, 96–100 (2018).
21. Y. Tajitsu, T. Masuda, T. Furukawa, *Jpn. J. Appl. Phys.* **26**, 1749–1753 (1987).
22. E. Bellet-Amalric, J. F. Legrand, *Eur. Phys. J. B* **3**, 225–236 (1998).
23. D. W. Fu *et al*., *Science* **339**, 425–428 (2013).
24. H. Y. Ye *et al*., *Science* **361**, 151–155 (2018).
25. Y. J. Park *et al*., *Appl. Phys. Lett.* **88**, 242908 (2006).
26. J. S. Lee, A. A. Prabu, K. J. Kim, *Polymer (Guildf.)* **51**, 6319–6333 (2010).
27. F. J. Boerio, J. L. Koenig, *Polymer Phys.* **9**, 1517–1523 (1971).
28. M. Kobayashi, K. Tashiro, H. Tadokoro, *Macromolecules* **8**, 158–171 (1975).
29. Materials and methods are available as supplementary materials.
30. I. I. Naumov, L. Bellaiche, H. Fu, *Nature* **432**, 737–740 (2004).
31. H. Schmid, *J. Phys. Condens. Matter* **20**, 434201 (2008).
32. S. Prosandeev *et al*., *Phys. Rev. B* **87**, 195111 (2013).
33. M. Guo *et al*., *Adv. Sci.* **6**, e1801931 (2019).
34. A. G. Shtukenberg, Y. O. Punin, A. Gujral, B. Kahr, *Angew. Chem. Int. Ed.* **53**, 672–699 (2014).
35. E. M. Woo, G. Lugito, *Eur. Polym. J.* **71**, 27–60 (2015).
36. B. Crist, J. M. Schultz, *Prog. Polym. Sci.* **56**, 1–63 (2016).
37. P. Poudel, S. Majumder, S. Chandran, H. Zhang, G. Reiter, *Macromolecules* **51**, 6119–6126 (2018).
38. S. Nurkhamidah, E. M. Woo, *Macromol. Chem. Phys.* **214**, 673–680 (2013).
39. Z. Wang *et al*., *Macromolecules* **40**, 4381–4385 (2007).
40. J. S. Bangsund *et al*., *Nat. Mater.* **18**, 725–731 (2019).
41. R. H. Gee, L. E. Fried, *J. Chem. Phys.* **118**, 3827–3834 (2003).
42. T. Yagi, M. Tatemoto, J. Sako, *Polym. J.* **12**, 209–223 (1980).
43. Y. Liu *et al*., *Nat. Mater.* **19**, 1169–1174 (2020).
44. A. J. Lovinger, T. Furukawa, G. T. Davis, M. G. Broadhurst, *Polymer (Guildf.)* **24**, 1225–1232 (1983).
45. A. R. Damodaran, E. Breckenfeld, Z. Chen, S. Lee, L. W. Martin, *Adv. Mater.* **26**, 6341–6347 (2014).
46. K. Tashiro, K. Takano, M. Kobayashi, Y. Chatani, H. Tadokoro, *Ferroelectrics* **57**, 297–326 (1984).
47. Z. Zhang, M. H. Litt, L. Zhu, *Macromolecules* **50**, 9360–9372 (2017).
48. Y. Liu, Z. Han, W. Xu, A. Haibibu, Q. Wang, *Macromolecules* **52**, 6741–6747 (2019).
49. Q. M. Zhang, V. Bharti, X. Zhao, *Science* **280**, 2101–2104 (1998).
50. S. Bauer *et al*., *Sens. Actuator A Phys.* **37-38**, 497–501 (1993).

51. T. D. Binnie, H. J. Weller, Z. He, D. Setiadi, *IEEE Trans. Ultrason. Ferroelectr. Freq. Control* **47**, 1413–1420 (2000).
52. A. Hassani, M. Skorobogatiy, *Opt. Express* **16**, 20206–20214 (2008).
53. J. Petzelt *et al*., *Phys. Status Solidi. A Appl. Mater. Sci.* **210**, 2259–2271 (2013).
54. A. P. Mosk, A. Lagendijk, G. Lerosey, M. Fink, *Nat. Photonics* **6**, 283–292 (2012).
55. S.-Q. Li *et al*., *Science* **364**, 1087–1090 (2019).
56. B. Ferguson, X.-C. Zhang, *Nat. Mater.* **1**, 26–33 (2002).
57. M. Lee *et al*., *Science* **298**, 1401–1403 (2002).
58. S. Koenig *et al*., *Nat. Photonics* **7**, 977–981 (2013).

ACKNOWLEDGMENTS

We thank Z. Dan, Y. Liang, W. Wang, and S. Ren for helpful discussions and the Electron Microscopy Laboratory at Peking University for the use of electron microscopes. This research used resources at the Advanced Photon Source, a U.S. Department of Energy (DOE) Office of Science User Facility operated for the DOE Office of Science by Argonne National Laboratory under contract no. DE-AC02-06CH11357. **Funding:** This work was supported by the Basic Science Centre Program of NSFC (grant no. 51788104), the NSF of China (grant no. 51625202), and the National Key Research & Development Program (grant no. 2017YFB0701603). L.-Q.C. knowledges support from the Hamer Foundation for the Hamer Professorship. **Author contributions:** M.G. and Y.S. conceived and performed the experiments. M.G., S.H., and T.T. fabricated the films. J.H. and B.X. performed the first-principle computations. C.G., H.H., and L.-Q.C. performed the phase-field simulations. S.C. and P.G. performed the TEM measurements. M.G., K.W., and J.M. performed the PFM measurements. Q.L. and J.S. performed the WAXS measurements. M.G. and S.H. conducted the dielectric and ferroelectric measurements. M.G. and D.Y. performed the AFM-IR measurements. M.G. wrote the first draft of the manuscript. Y.S., S.Z., Y.-H.L., and C.-W.N. revised the manuscript. All authors discussed the results and edited the manuscript. **Competing interests:** The authors declare no competing interests. **Data and materials availability:** All relevant data are available in the main text or the supplementary materials.

SUPPLEMENTARY MATERIALS

science.sciencemag.org/content/371/6533/1050/suppl/DC1
Materials and Methods
Supplementary Text
Figs. S1 to S33
Tables S1 and S2
References (*59*–*68*)

26 April 2020; resubmitted 25 May 2020
Accepted 14 January 2021
10.1126/science.abc4727

Toroidal polar topology in strained ferroelectric polymer

Mengfan Guo, Changqing Guo, Jian Han, Shulin Chen, Shan He, Tongxiang Tang, Qian Li, Joseph Strzalka, Jing Ma, Di Yi, Ke Wang, Ben Xu, Peng Gao, Houbing Huang, Long-Qing Chen, Shujun Zhang, Yuan-Hua Lin, Ce-Wen Nan, and Yang Shen

Science, **371** (6533), .
DOI: 10.1126/science.abc4727

Polarization hits a bull's-eye

Polymer-based ferroelectric materials are attractive because they can be solution processed cheaply and have much greater flexibility than ceramics. Guo *et al.* found concentric circular bands of polarization in a ferroelectric polymer that look like a bull's-eye target (see the Perspective by Martin). This self-organized toroidal texture is aligned perpendicularly to the axis of the polymer chains, allowing the authors to demonstrate selective absorption of infrared radiation and manipulation of terahertz radiation. This distinct structure in a polymer could be of interest for exploring and using other exotic effects.

Science, this issue p. 1050; see also p. 992